Materials Horizons

ROYAL SOCIETY OF CHEMISTRY

COMMUNICATION

View Article Online
View Journal

Cite this: DOI: 10.1039/d5mh01978h

Received 18th October 2025,
Accepted 28th January 2026

DOI: 10.1039/d5mh01978h

rsc.li/materials-horizons

Thermal rectification of shape memory polymer composites by programmable conductivity modulation

Seongkyun Kim,†[a] Dohyeong Lee,†[a] Seonghyun Bae,[a] Yongseok Jeong,[b] Minju Jeong,[c] Changsik Song [b] and Seunghyun Baik *[a]

The temperature-dependent thermal conductivity (κ) variation has been actively investigated as a thermal rectification mechanism. However, the intrinsic κ modulation of solid materials is limited. Here we report a shape memory polymer composite (SMPC) by combining the shape-changing ability of cross-linked poly(ethylene-*co*-vinyl-acetate) with the electrical/thermal functions of silver flakes. The matrix polymer volume change, in contrast to the constant silver flake volume, significantly modulates the volumetric filler fraction during the programming–recovery process. This results in a large change in electrical conductivity (210%) and κ (88%) between 20 and 100 °C, which is employed as a novel thermal rectification mechanism. Only a quarter of the SMPC is partially programmed to realize asymmetry in thermomechanical response. The thermal rectification efficiency (TR) increases as the heat transfer rate and temperature difference across the specimen (ΔT) increase, reaching 38.3% at 0.15 W and 73.4% at ΔT = 45 °C. The SMPC exhibits the highest TR at a significantly smaller ΔT compared with the data in the literature.

New concepts

The temperature-dependent thermal conductivity (κ) variation is a promising mechanism to realize thermal rectification. However, the intrinsic κ modulation of conventional solid materials is typically limited. Here we significantly increase the κ variation of a shape memory polymer composite (SMPC) by modulating the volumetric filler fraction to achieve high thermal rectification efficiency (TR). Cross-linked poly(ethylene-*co*-vinyl-acetate) is employed as a shape memory polymer matrix, which shows a large programmable volume change depending on temperature. In contrast, the volume of thermally conductive silver flake fillers is invariant, resulting in a large change in volumetric filler fraction. This dramatically modulates κ, resulting in a high TR (73.4% at ΔT = 45 °C). The SMPC exhibits the highest TR at a significantly smaller ΔT compared with the data in the literature.

Introduction

Advanced thermal management technology has received considerable attention recently as the integration density of electronic and energy devices increases.[1–3] Thermal rectification is an asymmetric heat transfer phenomenon depending on the direction of the temperature gradient, where the thermal conductance in the forward direction is higher than that in the reverse direction.[4–6] It shows great potential for applications in thermal diodes, thermal transistors, thermal logic gates, and directional heat dissipation/insulation in energy-efficient buildings.[7–10] Various mechanisms have been investigated to realize thermal rectification, including the temperature-dependent thermal conductivity (κ) variation,[11–15] phase change,[16–21] phonon localization,[22–24] asymmetric elastic modulus,[4,25] and asymmetric thermal radiation.[5,6] Although a relatively high thermal rectification efficiency (TR) was reported using nanoscale devices, a new mechanism still needs to be developed for practical bulk-scale applications.[26–29]

Previous thermal rectification studies based on the temperature-dependent κ variation primarily relied on the intrinsic κ modulation of metal, oxide, carbon, and ceramic materials.[11–15] However, the intrinsic κ modulation range was relatively limited, and a large temperature difference (*e.g.*, $\Delta T > 200$ K) was required to achieve a high TR.[11–15] Metallic particles such as silver (Ag), gold (Au), copper (Cu), and aluminum (Al) show only a little change in κ ($\leq$1.5%) between 20 and 100 °C, for instance.[30,31] A relatively large κ modulation could be achieved using phase change materials.[16–21] However, the κ modulation occurs only around the phase change temperature, confining the device to a narrow operating temperature window. The fabrication of heterostructures, by joining materials with distinctively different temperature-dependent κ modulation, is also challenging due to

[a] School of Mechanical Engineering, Sungkyunkwan University, Suwon, 16419, Republic of Korea. E-mail: sbaik@skku.edu
[b] Department of Chemistry, Sungkyunkwan University, Suwon, 16419, Republic of Korea
[c] School of Chemical Engineering, Sungkyunkwan University, Suwon, 16419, Republic of Korea
† These authors contributed equally.

the complex synthesis process.[14] The joining process may need high-temperature processing. Besides, the risk of junction failure increases due to mechanical instability at the interface of joined dissimilar materials, limiting practical applicability.[32]

Shape memory polymers (SMPs) are smart materials that can be deformed and fixed into a temporary shape, then recover their original permanent shape through programmed strain recovery. They return to the original shape in response to external stimuli, such as heat,[33–35] light,[36] electric field,[37] and moisture.[38] SMPs have been explored for applications in various fields, including medical treatment, soft robotics, flexible electronics, and automotive/aerospace industry.[39–41] However, SMPs are typically insulating or exhibit very small κ and electrical conductivity (σ), restricting their use in applications requiring active thermal and electrical functions. Shape memory polymer composites (SMPCs) have received much attention for reinforcing and expanding the properties of SMPs.[42–44] These composites combine the shape-changing ability of SMPs with the functional properties of reinforcing fillers. The fillers can enhance mechanical properties or impart electrical/thermal functions.[42,45] For example, high-κ fillers such as carbon nanotubes (CNTs) were introduced to improve the thermal properties of SMPCs. However, the enhancement was limited, and the κ value of the SMPC was only $\sim$1 W m^{-1} K^{-1}.[46]

The deformation between the temporary and permanent shapes of the SMPC changes the total volume of the composite. However, the volume of solid fillers is invariant during the shape change, modulating the volumetric filler fraction (*i.e.*, filler volume/composite volume). Here we employ the volumetric filler fraction modulation to control the κ of the SMPC and realize thermal rectification. A crystalline polymer, poly(ethylene-*co*-vinyl-acetate) (PEVA), is cross-linked with dicumyl peroxide (DCP) as a matrix material to induce shape memory characteristics upon temperature modulation. Silver flakes (AgFLs) are incorporated as conductive fillers to impart electrical and thermal functions to the SMPC. The percolation theory suggests the modulation of σ and κ in response to the change in volumetric filler fraction. The SMPC shows a large change in both σ (210%) and κ (88%) between 20 and 100 °C due to the temperature-dependent modulation of volumetric filler fraction, which is employed as a novel thermal rectification mechanism. Only a quarter of the SMPC is partially programmed to realize asymmetry in the thermomechanical response of the specimen. A unique experimental setup is developed to measure TR during the volume change of the SMPC. The TR increases as the heat transfer rate increases, reaching 38.3% at 0.15 W. The TR also increases as the temperature difference between the two ends of the SMPC (ΔT) increases. It reaches as high as 73.4% at ΔT = 45 °C. The SMPC exhibits the highest TR at a significantly smaller ΔT compared with the literature data employing the temperature-dependent κ variation as a thermal rectification mechanism. The σ and κ show reversible modulation from the 2nd programming–recovery cycle ($\sigma_{recovered}/\sigma_{programmed}$ = 3.15 and $\kappa_{recovered}/\kappa_{programmed}$ = 1.83) although incomplete recovery is observed for the 1st cycle.

Results

The thermal conductivity variation mechanism of the SMPC during the programming and recovery processes

Fig. 1a illustrates the working principle of the SMPC. A detailed synthesis process is provided in the Methods section. The blue dashed box indicates the programming process of the SMPC. A substantial volume change is achieved in response to the temperature variation by employing SMP as the matrix material. PEVA is used as the matrix material, which exhibits the shape memory effect after crosslinking.[35] The molecular structure of PEVA consists of actuation chains and cross-linking sites. The cross-linking sites enhance thermal stability at elevated temperatures and strengthen the shape memory effect by reinforcing the matrix structure.[35] The AgFLs are also embedded in the PEVA matrix to enhance both κ and σ. A scanning electron microscopy (SEM) image of the AgFLs and size distribution analysis are provided in Fig. S1, SI. The average size of the AgFLs is 4.37 μm. The as-prepared SMPC exhibits the random orientation of crystalline chains (Fig. 1a-i). Heating above the melting temperature (T_m) induces the transition of actuation chains from crystalline to amorphous (*i.e.*, liquid-like disordered) states, enabling the SMPC to deform into a temporary shape (Fig. 1a-ii). The SMPC is mechanically stretched at this state, aligning the polymer chains along the direction of applied stress. In the next step, the SMPC is cooled under tensile stress (Fig. 1a-iii). The amorphous chain transforms into an oriented crystalline structure in the stretched direction when the SMPC is cooled below the crystallization temperature (T_c). The tensile stress is then released. The formation of crystalline chains allows the SMPC to maintain the internal stress and temporary shape. The red dashed box represents the recovery process (Fig. 1a-iv). The SMPC is reheated above T_m, enabling the PEVA chains to deform again. The SMPC contracts back to its initial shape in the amorphous state due to the stored internal stress.[33,35] Finally, the PEVA chain returns to the randomly oriented crystalline structure upon cooling to room temperature. The crystalline structure change is a critical process to induce the shape memory effect.[35]

The thermodynamic characteristics of the SMPC, with and without cross-linking, are analyzed by differential scanning calorimetry (DSC) analysis (Fig. 1b). The cross-linking of PEVA decreases both T_m and T_c. The degree of crystallinity (X_c) is also decreased from 31 to 27% after cross-linking (eqn (1)).

$$X_c = \frac{\Delta H_m}{\Delta H_{m,\infty}} \times 100\ (\%) \quad (1)$$

where ΔH_m is the measured enthalpy of fusion and $\Delta H_{m,\infty}$ is the enthalpy of fusion of a perfect polyethylene (PE) crystal.[47,48] PEVA is composed of two distinct phases: a crystalline phase derived from PE segments and an amorphous phase originating from vinyl acetate (VA) units. The synthesis of PEVA involves the incorporation of VA into the PE backbone, which imparts rubber-like properties.[48] The thermodynamic properties of the SMPC, with and without the cross-linker, are

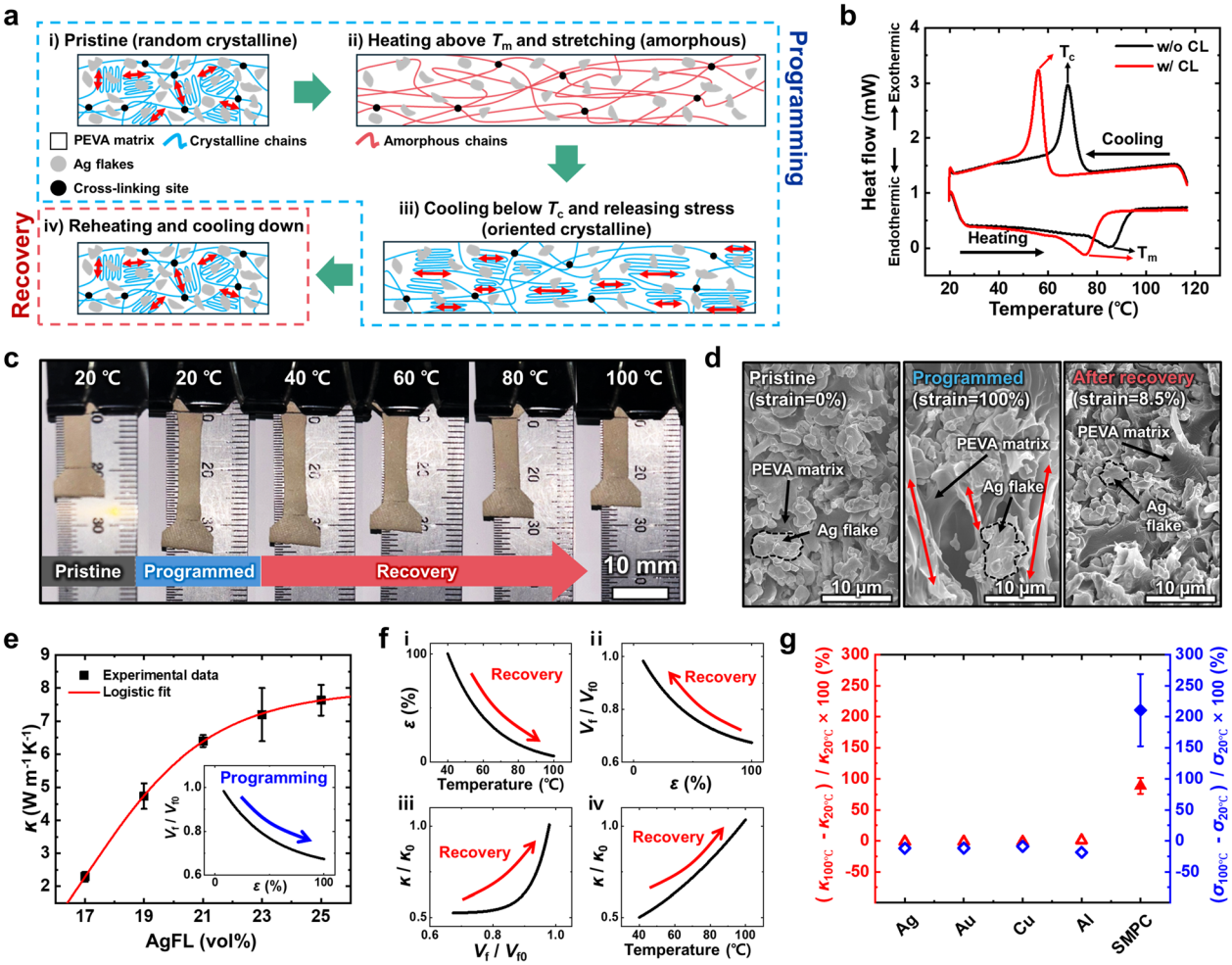

Fig. 1 The thermal conductivity variation mechanism of the SMPC during the programming and recovery processes. (a) The working principle of the SMPC. The programming and recovery processes are indicated by blue and red boxes, respectively. (b) DSC analysis of the SMPC with and without crosslinking. (c) The optical images of the pristine, programmed, and recovered SMPCs. All the images are taken after cooling to 20 °C at each step. (d) Cross-sectional SEM images of the pristine, programmed (ε = 100%), and recovered (strain = 8.5%) SMPCs. The red arrow indicates the elongated matrix polymer. The concentration of AgFLs is 25 vol%. (e) The thermal conductivity of the SMPC as a function of AgFL concentration. The data are fitted to a logistic regression model, and the regression error (R^2) is 0.9998. The filler fraction is decreased during the programming (*i.e.*, stretching) stage, resulting in a decrease in thermal conductivity (inset). (f) The thermal conductivity restoration mechanism during the recovery process. The strain of the programmed (*i.e.*, stretched) SMPC is decreased as the temperature increases (i), resulting in an increase in the filler fraction (ii). This increases thermal conductivity (iii). Overall, the thermal conductivity increases to the initial value (*i.e.*, the conductivity of the pristine SMPC) as the temperature increases (iv). (g) The experimentally measured thermal and electrical conductivity variations of the SMPC and metals between 20 and 100 °C.

summarized in Table S1, SI. The covalent bonding by the crosslinker DCP restricts crystal growth, decreasing T_m, T_c, and X_c. The cross-linked sites act as net-points retaining the internal stress within the SMPC, while the crystalline chains function as switching segments.[35,49] Thus, the cross-linking plays a vital role in shape memory function, although it shortens the effective chain length and decreases crystallinity.[35] Note that the endothermic melting peak of the cross-linked SMPC disappears at 88 °C, and the programming and recovery processes are carried out at 100 °C, as discussed later. The incorporation of AgFLs into the cross-linked PEVA matrix increases tensile strength but decreases rupture strain (Fig. S2, SI).

Fig. 1c shows the optical images of the SMPC during the programming and recovery process. The as-prepared pristine SMPC is imaged at 20 °C. The SMPC is programmed by heating to 100 °C, stretching, and cooling to 20 °C (see the Methods section for details). The axial tensile strain (ε) of the elongated SMPC is 100% after programming. In the next step, the SMPC is heated stepwise (40, 60, 80, and 100 °C) in order to demonstrate the shape change during the recovery process. All the images are taken after cooling to room temperature at each step. The AgFLs are uniformly distributed (25 vol%) in the pristine SMPC as shown in the SEM image (Fig. 1d, pristine). The programmed SMPC (ε = 100%) shows elongated polymer chains and increased distance between AgFLs along the stretched direction (Fig. 1d, programmed). The specimen returns to the initial shape after heating to 100 °C (Fig. 1d, after recovery), although the strain is incompletely recovered during the 1st programming–recovery cycle, as discussed later. The filler distribution is also confirmed by the electrical transport measurement

(Fig. S3, SI). The pristine and recovered SMPCs show nearly isotropic σ. In contrast, the longitudinal σ is smaller than the transverse σ for the programmed SMPC due to the non-uniform filler distribution. A more detailed electrical transport analysis is presented in Fig. 2.

Fig. 1e shows the κ of the SMPC as a function of the volumetric filler fraction (V_f).

$$V_f = \frac{V_{filler}}{V_{composite}} \quad (2)$$

where V_{filler} is the volume of AgFLs and $V_{composite}$ is the entire volume of the SMPC. The κ increases with increasing V_f due to the effective percolation network construction, demonstrating saturation behavior (κ = 7.6 W m^{-1} K^{-1}) at V_f = 25%. The σ of the SMPC also increases as V_f increases (Fig. S4, SI). The inset of Fig. 1e shows the change in volumetric filler fraction (V_f/V_{f0}) as a function of ε, during the programming process, where V_{f0} is the volumetric filler fraction before stretching. The V_f/V_{f0} decreases as ε increases, because $V_{composite}$ increases during stretching, whereas V_{filler} is invariant.[50] Note that the experimentally measured Poisson's ratio (ν) of the SMPC is 0.38, and $\Delta V_{composite}/V_{composite} = (1-2\nu) \times \varepsilon$ for a rectangular specimen. The V_f becomes 16.9% at ε = 100%. The AgFL conduction pathways become unconnected as V_f/V_{f0} decreases, reducing the κ of the SMPC. Note that the Bruggeman model (effective medium theory), which treats both the matrix and filler phases symmetrically within the same effective medium, underestimates the κ of the SMPC (see the SI for details).[51] The theoretically calculated κ is only 0.42 W m^{-1} K^{-1} at V_f = 17%, whereas the experimentally measured κ is 2.3 W m^{-1} K^{-1}. This implies that the percolation network is still partially operative even at V_f = 17%. The modulation mechanism of κ during the recovery process is illustrated in Fig. 1f. The ε of the programmed (*i.e.*, elongated) SMPC decreases as the temperature increases (Fig. 1f-i), resulting in an increase in V_f/V_{f0} (Fig. 1f-ii). This increases κ (Fig. 1f-iii). Overall, the κ increases towards the initial value as the temperature increases (Fig. 1f-iv). Note that the κ of the SMPC is also affected by other factors during the programming–recovery process, in addition to V_f, as discussed later.

Fig. 1g compares the modulation of the κ and σ of the SMPC and conventional conductive metals, such as Ag, Au, Cu, and Al. The conventional conductive metals show only a little change in κ ($\lesssim$1.5%) and σ ($\lesssim$18.4%) between 20 and 100 °C.[30,31] In contrast, the SMPC shows a significantly greater change in both κ (88%) and σ (210%). This large conductivity modulation between 20 and 100 °C is employed as a novel thermal rectification mechanism, as discussed later.

The experimentally measured electrical and thermal conductivity variation of the SMPC during the programming and recovery processes

The σ and κ of the SMPC are experimentally measured during the programming and recovery processes. Fig. 2a shows the σ and V_f as a function of ε. The σ is measured by the four-point probe method.[52] The ε is increased to 100% during the

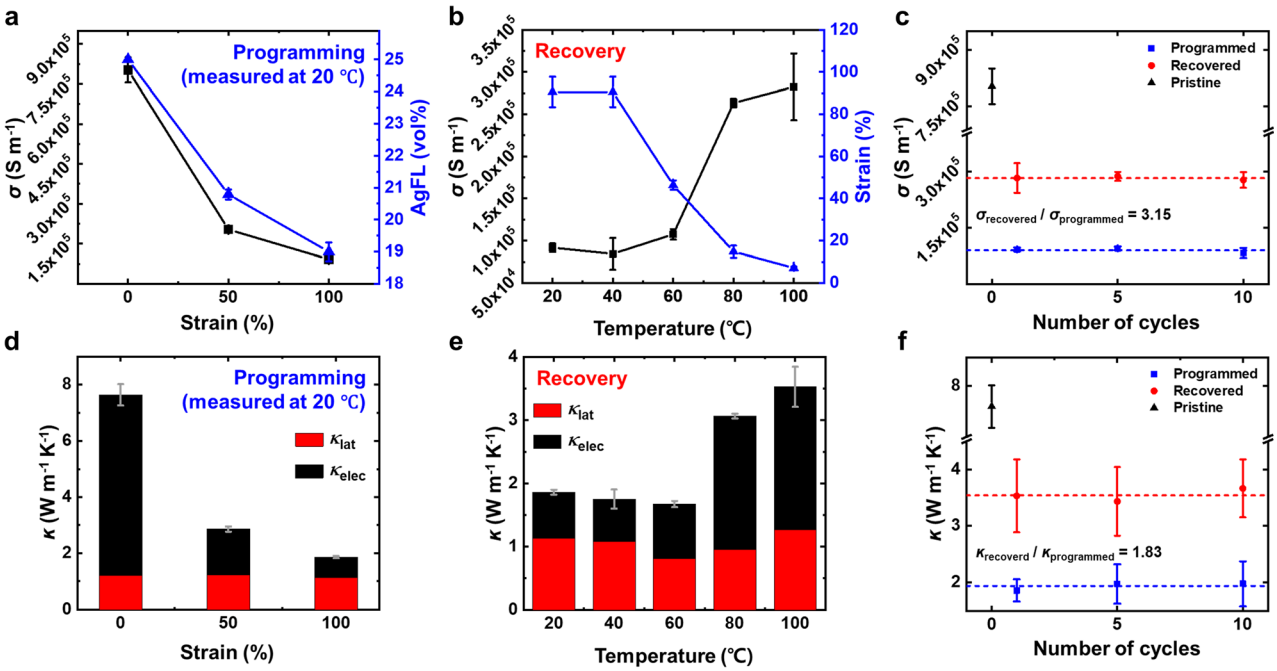

Fig. 2 The experimentally measured electrical and thermal conductivity variations of the SMPC during the programming and recovery processes. (a) The electrical conductivity and AgFL concentration as a function of programming strain. The error bar represents the standard deviation of the data. (b) The electrical conductivity and strain as a function of reheating temperature during the recovery process. (c) The electrical conductivity as a function of the number of programming–recovery cycles. (d) The thermal conductivity as a function of programming strain. The total thermal conductivity is divided into lattice thermal conductivity and electronic thermal conductivity ($\kappa = \kappa_{lat} + \kappa_{elec}$). (e) The thermal conductivity as a function of reheating temperature during the recovery process. (f) The thermal conductivity as a function of the number of programming–recovery cycles.

programming process, resulting in a decrease in V_f due to the increase in $V_{composite}$ as discussed earlier. Consequently, the σ of the SMPC decreases significantly. The ε is increased at 100 °C during the programming process, and the σ is measured after cooling the specimen to 20 °C at each strain.

Fig. 2b shows the change in the σ and ε of the programmed SMPC during the recovery process. The recovery process is carried out by increasing the temperature from 20 to 100 °C in steps of 20 °C. The ε begins to decrease when the temperature is increased beyond 40 °C, where the onset of the endothermic melting peak is observed in DSC analysis (Fig. 1b). The decrease in ε increases V_f and σ, as shown in Fig. 1f. The σ is measured after cooling the specimen to 20 °C at each heating step. The σ starts to increase more rapidly as the temperature is increased beyond 60 °C, where the melting peak distinctly increases (Fig. 1b). However, the σ does not fully return to its initial value even when the SMPC is heated to 100 °C. This could be due to the incomplete strain recovery of the SMPC during the 1st programming–recovery cycle. The orientation, interparticle distance, and percolation network of the AgFLs do not completely return to the initial states, resulting in incomplete σ recovery. The σ shows reversible modulation between the programmed and recovered states after the 1st cycle (Fig. 2c). There is no change in the σ modulation ($\sigma_{recovered}/\sigma_{programmed} = 3.15$) up to 10 programming–recovery cycles. Note that the SMPC is heated to 100 °C and stretched at each programming step. A more detailed mechanism for the conductivity modulation will be discussed below.

Fig. 2d shows the κ variation of the SMPC during the programming process. The κ is calculated as $\kappa = \alpha\rho C_p$, where α is the thermal diffusivity measured by the laser flash method, ρ is the density, and C_p is the specific heat capacity.[53,54] The properties are measured after cooling the specimen to 20 °C at each strain. The α and ρ are provided as a function of ε in Fig. S5, SI. The decrease in V_f with increasing ε results in a decrease in both α and ρ. This leads to a decrease in κ. The C_p shows little variation with strain.

The κ can be divided into lattice thermal conductivity (κ_{lat}) and electronic thermal conductivity (κ_{elec}).[53–55]

$$\kappa = \kappa_{lat} + \kappa_{elec} \quad (3)$$

The κ_{elec} is calculated using the Wiedemann–Franz law ($\kappa_{elec} = L\sigma T$), where L is the Lorenz number and T is the absolute temperature.[54–56] The Sommerfeld constant (2.44×10^{-8} V^2 K^{-2}) is adopted for L as an approximation due to the high σ of the SMPC.[57] Previous studies have demonstrated that the Sommerfeld constant can be reasonably employed for the transport analysis of polymer composites, when the electrical conductivity and carrier concentration are sufficiently high, since free electrons dominate the transport process under such conditions.[57] The κ_{lat} remains nearly constant during the programming process, while κ_{elec} decreases with increasing ε. This demonstrates that the dominant factor influencing the κ variation is the network of AgFLs rather than the polymer matrix. Since electrons are dominant thermal carriers in metals, the strain-induced variation in V_f primarily affects σ and κ_{elec}. In contrast, the variation in κ_{lat} remains relatively small.

Fig. 2e shows the κ of the SMPC during the recovery process. The κ starts to increase when the temperature is increased beyond 60 °C, similar to the σ variation trend (Fig. 2b). The recovery mostly happens in κ_{elec}, while κ_{lat} exhibits little change. The modulation of σ, κ_{elec}, and κ during the programming and recovery process is primarily governed by the AgFL pathways, rather than the phonons of the polymer matrix. The κ does not fully recover to its original value when the SMPC is heated to 100 °C.

Fig. 2f shows the κ variation during 10 programming–recovery cycles. The κ shows reversible modulation between the programmed and recovered states ($\kappa_{recovered}/\kappa_{programmed} = 1.83$) after the 1st cycle, similar to the σ variation trend. Incomplete strain recovery is observed during the 1st cycle due to the irreversible microstructure rearrangement of the SMPC (Fig. S6, SI). Polymer chain reorientation and stress relaxation were observed during the 1st stretching cycle of polymer–matrix composites in the literature.[58,59] This would change the filler orientation, interparticle distance, filler network connectivity/percolation, and the thermal contact resistance between fillers. These factors would also affect the κ of the SMPC, in addition to V_f, as ε varies during the programming–recovery process. As a result, incomplete recovery of the ε and κ of the SMPC is observed during the 1st cycle. This behavior is reduced and both ε and κ show reversible modulation from the 2nd cycle onward.

The thermal rectification of the SMPC

The thermal rectification experiment is carried out using a laboratory-built setup (Fig. 3a).[6] An optical image of the experimental setup is provided in Fig. S7, SI. A vacuum chamber ($\sim 10^{-3}$ Torr) equipped with a zinc selenide (ZnSe) window is employed to avoid convection heat transfer.[55] The SMPC is suspended between two nickel (Ni) plates using fastening bolts. Ni is selected due to its high κ, mechanical strength, and rigidity. The surface is coated with graphite for accurate temperature measurement using an infrared (IR) camera. The reflection temperature and emissivity are calibrated following ASTM standards (Fig. S8a, SI).[5,6,60,61] A nearly uniform emissivity of ~ 0.84 is observed for the graphite-coated SMPC and Ni plate, which is not sensitive to temperature variations (Fig. S8b, SI). Cartridge heaters are inserted into the Cu blocks. One side is heated at a time, and the other side acts as a heat sink. The left Cu block is placed on a moving stage connected to a stepper motor, which adjusts position in response to the strain variation of the SMPC. Note that the stepper motor is carefully controlled in order not to apply any additional external force on the SMPC. The SMPC is elongated during the programming process and then mounted on the Cu block without inducing any additional strain. The stage is moved in the next step, loosening the SMPC, and then the recovery process is carried out by changing the temperature. Finally, the SMPC becomes

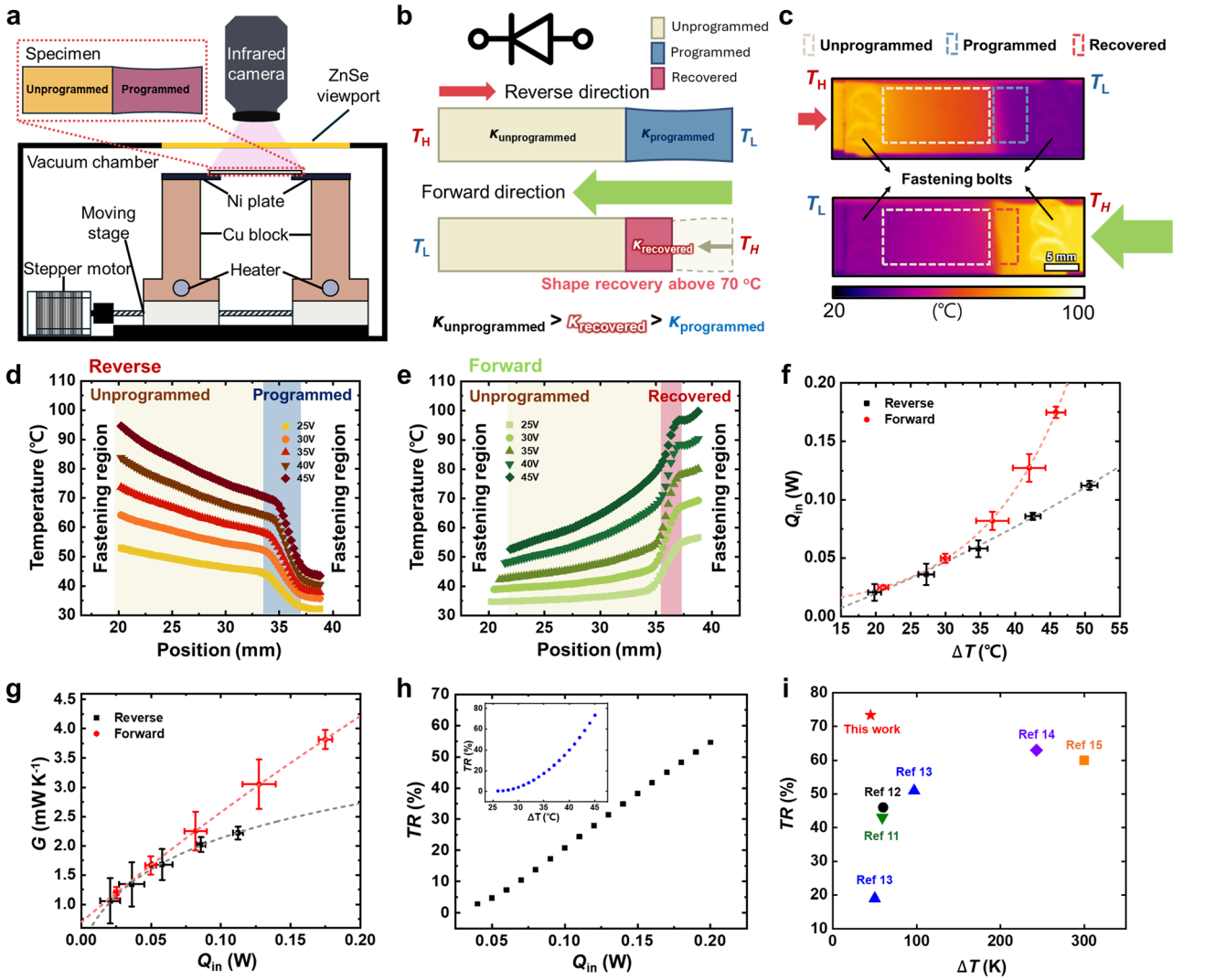

Fig. 3 The thermal rectification of the SMPC. (a) Schematic of the thermal rectification experimental setup. The SMPC is suspended between two Ni plates which are placed on Cu blocks. The cartridge heaters are inserted into the Cu blocks. One side is heated at a time, and the other side acts as a heat sink. The left Cu block is placed on a moving stage connected with a stepper motor to match the strain change of the SMPC. (b) The thermal rectification mechanism of the SMPC. The left side of the specimen is pristine (*i.e.*, unprogrammed), and only the right side is programmed ($\varepsilon/\varepsilon_0$ = 2), as shown in the top image. The bottom image shows the specimen after recovery by heating above 70 °C. The reverse and forward heat flow directions are indicated by red and green arrows, respectively. (c) Infrared camera images of the SMPC during the reverse and forward heat flow experiments (heating voltage = 35 V). The fastening bolts are also shown. (d) and (e) The temperature profiles of the SMPC during the reverse and forward heat flow experiments. (f) The input heat transfer rate (Q_{in}) is shown as a function of the temperature difference between the two ends of the SMPC (ΔT). The data are fitted to exponential regression models ($R^2_{reverse}$ = 0.9961 and $R^2_{forward}$ = 0.9998). The error bar represents the standard deviation of the data. (g) The thermal conductance (G) is shown as a function of Q_{in}. The data are fitted to logarithmic regression models ($R^2_{reverse}$ = 0.9952 and $R^2_{forward}$ = 0.9999). (h) The thermal rectification efficiency (TR) is shown as a function of Q_{in} or ΔT (inset). The TR is calculated using the regression data. (i) The comparison of the TR of the SMPC with the data in the literature. Only the experimentally obtained TR values are compared.

flat again, after the recovery process, by readjusting the stage position.

Fig. 3b shows the thermal rectification mechanism of the SMPC. The SMPC is partially programmed to induce the direction-dependent thermal conductance (G) modulation. Only a quarter of the SMPC on the right side is clamped, heated to 100 °C for 10 minutes, and stretched to 100% strain using a laboratory-built setup. It is then cooled to room temperature at 100% strain. The programmed region is maintained at a lower temperature when heat flows from the unprogrammed region to the programmed region (Fig. 3b, top). The left end of the SMPC is maintained at a higher temperature. The corresponding IR image is shown in Fig. 3c (top). The white and blue dashed boxes indicate the unprogrammed and programmed regions, respectively. The fastening regions with bolts are also shown at the far left and right ends of the specimen. The recovery (*i.e.*, contraction) of the programmed region is suppressed due to the relatively low temperature, maintaining the low κ of the programmed region. As a result, the entire SMPC exhibits a relatively lower average G.

This heat flow direction (unprogrammed → programmed) is referred to as the reverse direction. In contrast, the programmed region is maintained at a higher temperature when heat flows from the programmed region to the unprogrammed region (forward direction), as shown in Fig. 3b (bottom). The programmed region undergoes the recovery process when the temperature is increased above T_m. The corresponding infrared image is shown in Fig. 3c (bottom). The contracted recovered region is indicated by the red dashed box. The recovered region has a higher κ compared with the programmed region. Therefore, a relatively higher average G is induced for the entire SMPC, realizing thermal rectification. Fig. S9 (SI) compares the experimentally measured κ of the programmed and unprogrammed SMPCs as a function of temperature. The κ of the programmed SMPC increases when the temperature increases beyond 60 °C, as shown in Fig. 2e. However, the κ of the unprogrammed SMPC remains relatively constant between 20 and 100 °C, without exhibiting the increasing trend.

Fig. 3d shows the temperature profiles of the SMPC in the reverse heat flow direction (unprogrammed → programmed). The cartridge heaters installed in the left copper block are heated by supplying voltage from 25 to 45 V in steps of 5 V. The right copper block is employed as a heat sink. The IR camera images of the SMPC, including fastening regions with Ni plates, are provided in Fig. S10, SI. The programmed SMPC is maintained at relatively low temperatures, suppressing the recovery process and maintaining its low κ. Fig. 3e shows the temperature profiles of the SMPC in the forward heat flow direction (programmed → unprogrammed). The right copper block is heated using cartridge heaters. The programmed region is maintained at significantly higher temperatures, resulting in shrinkage and increasing κ during the recovery process. The temperature profiles of two additional SMPC specimens are provided in Fig. S11, SI. All the SMPC specimens show a similar trend.

Fig. 3f shows the heat transfer rate input to the SMPC (Q_{in}) as a function of the temperature difference between two ends of the entire SMPC specimen ($\Delta T = T_H - T_L$). Three specimens are tested under each condition, and the mean values and standard deviations are presented. The ΔT is experimentally measured. The Q_{in} is obtained by the finite element method (FEM) analysis (see Fig. S12 in the SI for details). Only the fastening region, including the Ni plate and the inlet region of the SMPC, is simulated by the FEM. Experimentally measured temperatures at both ends of the fastening region are used as boundary conditions. Three-dimensional swept-hexahedron meshes are generated (mesh size = 250 μm), and both conduction and radiation heat transfer modes are considered in the simulation. The temperature-dependent κ and emissivity of the Ni plate and the SMPC are experimentally measured and used for the simulation. For simplicity, the fastening bolt itself is not considered in the FEM simulation. There is good agreement between the experimentally measured temperature profiles and simulation results, and Q_{in} is obtained from the simulation. The current mesh size (250 μm) is sufficient to obtain consistent Q_{in} as shown in the mesh convergence analysis (Fig. S13, SI). The Q_{in} in the forward direction is greater than that in the reverse direction at an equivalent ΔT when the heater voltage is higher than 30 V. In this case, the temperature of the programmed region is higher than 60 °C, triggering the recovery process and increasing κ.

Fig. 3g shows G as a function of Q_{in}. The G is calculated using eqn (4):[4–6]

$$G = \frac{Q_{in}}{\Delta T} = \frac{Q_{in}}{T_H - T_L} \quad (4)$$

The G in the forward direction becomes greater than that in the reverse direction at an equivalent Q_{in} when the heater voltage is increased beyond 30 V. The dashed line indicates a logarithmic fit to the experimental data. Note that it is difficult to precisely estimate G using the experimentally measured κ and specimen geometry, without the FEM simulation, since there is a temperature gradient inside the specimen during the rectification experiment. As shown in Fig. 3h, the TR is then calculated as a function of Q_{in} using the fitted data and eqn (5):[4–6]

$$TR = \frac{G_{forward} - G_{reverse}}{G_{reverse}} \times 100\ (\%) \quad (5)$$

The TR of the SMPC increases as Q_{in} increases, resulting in 38.3% at Q_{in} = 0.15 W. The TR of the SMPC is also shown as a function of ΔT (Fig. 3h, inset). The TR increases as ΔT increases, reaching 73.4% at ΔT = 45 °C. Fig. S14 (SI) shows the thermal rectification behavior during cyclic testing of the SMPC. Three thermal rectification cycles are investigated using the same specimen. The specimen is manually reprogrammed at the start of each thermal rectification cycle. It shows a repeatable TR of 29–39% at Q_{in} = 0.12 W (Fig. S14i (SI), inset). Note that there is a slight variation in TR as the programming is carried out manually, and this needs to be improved in the future.

Fig. 3i compares the TR of the SMPC with the data in the literature. The TR values are recalculated using eqn (5) from the thermal rectification reports with only the temperature-dependent κ variation mechanism.[11–15] Previous reports based on the κ modulation of phase change materials are not included for comparison since they operate only around the phase change temperature. Generally, the TR increases as ΔT increases. However, the SMPC shows the highest TR (73.4%) even at a significantly smaller ΔT (45 °C), demonstrating excellent thermal rectification behavior.

The PEVA-based SMPC needs reprogramming with external stress for each thermal rectification cycle. In order to overcome this limitation, a new SMPC is synthesized using polycaprolactone diol and polybutadiene diol (Fig. S15a, SI).[62,63] The T_m and T_c are observed to be 34.5 and −16.1 °C, respectively (Fig. S15b, SI). In this new SMPC, the external stress is applied only during the 1st programming process. It shows reversible length modulation only with temperature variation, without applying external stress, in the subsequent shape memory cycles (Fig. S15c, SI). It also shows reversible κ modulation although the variation is not large (Fig. S15d, SI). The κ variation needs to be improved

further in the future. The SMPC has thermal rectification and shape transformation characteristics. Thus, it may find applications in the outer surface of an electronic device, where preferential heat dissipation to the surrounding environment is desired while protecting the device when the environmental temperature exceeds the device temperature. The free end of the SMPC might be structured or connected to a thin fin to further enhance convective heat transfer with the surrounding environment.

Discussion

In summary, the V_f modulation of the SMPC during the programming and recovery processes is employed to control κ and realize thermal rectification. The shape memory ability of the cross-linked PEVA is combined with the electrical/thermal functions of AgFLs, realizing a large variation in both σ (210%) and κ (88%) between 20 and 100 °C. The σ and κ show reversible modulation from the 2nd programming–recovery cycle onward ($\sigma_{recovered}/\sigma_{programmed}$ = 3.15 and $\kappa_{recovered}/\kappa_{programmed}$ = 1.83). Only a quarter of the SMPC is partially programmed using a laboratory-built setup to realize asymmetry in the thermomechanical response of the specimen. The TR increases as Q_{in} and ΔT increase, reaching 38.3% at Q_{in} = 0.15 W and 73.4% at ΔT = 45 °C. The bulk-scale SMPC exhibits the highest TR at a significantly smaller ΔT compared with the data in the literature. The TR may be further improved in the future if the shape memory effect-induced κ variation of the SMPC is amplified by the intrinsic temperature-dependent κ variation of solid fillers.

Methods

Synthesis of the SMPC

The SMPC is synthesized by incorporating AgFLs into PEVA. Firstly, PEVA (Sigma-Aldrich, 340502, 1.5 g), DCP (Sigma-Aldrich, 329541, 5 wt%), and tetrahydrofuran (THF) without an inhibitor (Sigma-Aldrich, 18562, 25 mL) are mixed and heated in an oven (Jeio Tech, OF-02G-2C) at 60 °C for 3 hours. The AgFLs (Metalor, SA-31812, 17–25 vol%, 3.5372–5.787 g) are then dispersed in the PEVA solution with additional THF without an inhibitor (25 mL) using a centrifugal mixer (Thinky Co., ARE-310). The mixture is further stirred at 60 °C for 30 minutes in a heating mantle (MTOPS, MS-DMSDB631) to evaporate THF. Finally, it is completely dried in an oven at 60 °C for 12 hours and hot-pressed (QMESYS, QM900s) at 200 °C and 5 MPa for 1 hour to obtain the SMPC.

The programming and recovery processes of the SMPC

The SMPC is heated to 100 °C using a hot plate, and a quarter of the specimen is partially stretched using a laboratory-built setup. It is then cooled to room temperature (20 °C). In the next step, the SMPC is suspended between Ni plates using bolts and nuts in a vacuum chamber ($\sim 10^{-3}$ Torr) equipped with a ZnSe window. The recovery process is carried out by reheating the partially programmed SMPC stepwise (40, 60, 80, and 100 °C) using cartridge heaters inserted into the Cu blocks. The external stress of the specimen is removed by moving a stage attached to a stepper motor during the recovery process.

Characterization

Crystallization is investigated by differential scanning calorimetry (Hitachi, Nexta DSC 600). The morphology of the SMPC is examined by field-emission scanning electron microscopy (Hitachi, S-4800). The thermal diffusivity (α) is measured by the laser flash method (Netzsch, LFA 467). The density (ρ) is measured using the Archimedes method (Sartorius Quinitix224-1SKR). The specific heat capacity (C_p) is measured by differential scanning calorimetry (Netzsch, DSC214). The thermal conductivity (κ) is then calculated as $\kappa = \alpha\rho C_p$.[53] The electrical conductivity (σ) is measured by the four-point probe in-line method using a laboratory-built setup.[52,53] A nanovoltmeter (Keithley, 2182A) is used to measure the voltage drop along the specimen under a constant current (Keithley, 6221 DC supply). Thermal rectification is investigated using a laboratory-built setup.[6] The vacuum chamber ($\sim 10^{-3}$ Torr) is equipped with a ZnSe window, and the specimen temperature is monitored using an infrared camera (FLIR, A325sc). The reflected temperature and emissivity of the specimen are calibrated according to ASTM standards.[4,6,58,59]

Author contributions

Seongkyun Kim: conceptualization, data curation, investigation, methodology, validation, and writing – original draft. Dohyeong Lee: conceptualization, data curation, investigation, methodology, validation, and writing – original draft. Seonghyun Bae: data curation, methodology, and investigation. Yongseok Jeong: data curation, methodology, and investigation. Minju Jeong: data curation, methodology, and investigation. Changsik Song: data curation, methodology, investigation, validation, supervision, and funding acquisition. Seunghyun Baik: conceptualization, data curation, investigation, methodology, validation, writing – original draft, writing – review and editing, supervision, project administration, and funding acquisition.

Conflicts of interest

The authors declare no competing financial or non-financial interests.

Data availability

The authors declare that the main data supporting the findings of this study are available within the article and its supplementary information (SI). Supplementary information is available. See DOI: https://doi.org/10.1039/d5mh01978h.

All other relevant data are available from the corresponding author upon reasonable request.

Acknowledgements

This work was supported by the Samsung Research Funding & Incubation Center of Samsung Electronics under Project Number SRFC-MA2202-01, the Basic Science Research Program through the National Research Foundation of Korea (NRF) funded by the Ministry of Education (2021R1A6A1A03039696), and the "Carbon Upcycling Project for Platform Chemicals" (2022M3J3A1046019) through the NRF funded by the Ministry of Science and ICT, Republic of Korea.

Notes and references

1 Y. Li, W. Li, T. Han, X. Zheng, J. Li, B. Li, S. Fan and C.-W. Qiu, *Nat. Rev. Mater.*, 2021, **6**, 488–507.
2 M.-D. Li, X.-Q. Shen, X. Chen, J.-M. Gan, F. Wang, J. Li, X.-L. Wang and Q.-D. Shen, *Nat. Commun.*, 2022, **13**, 5849.
3 Y. Cui, Z. Qin, H. Wu, M. Li and Y. Hu, *Nat. Commun.*, 2021, **12**, 1284.
4 J. Lee, S. Cha, B. H. Lee, A. A. Jan, R. Kizhakkekara, J. Yang, M. K. Kim and S. Baik, *Mater. Horiz.*, 2023, **10**, 1431–1439.
5 J. Lee, A. A. Jan, S. P. Ganorkar, J. Cho, D. Lee and S. Baik, *Mater. Horiz.*, 2021, **8**, 1998–2005.
6 S. Kim, T. Kim, J. Sung, Y. Kim, D. Lee and S. Baik, *Mater. Horiz.*, 2023, **10**, 5720–5728.
7 L. Wang and B. Li, *Phys. Rev. Lett.*, 2007, **99**, 177208.
8 L. Castelli, Q. Zhu, T. J. Shimokusu and G. Wehmeyer, *Nat. Commun.*, 2023, **14**, 393.
9 X. Yang, S. Wang, C. Wang, R. Lu, X. Zheng, T. Zhang, M. Liu, J. Zheng and H. Chen, *ACS Appl. Mater. Interfaces*, 2022, **14**, 4434–4442.
10 H. Zhao, Y. Wu, H. Sun, B. Lin, M. Zhong, G. Jiang and S. Wu, *Renewable Energy*, 2023, **218**, 119278.
11 W. Kobayashi, Y. Teraoka and I. Terasaki, *Appl. Phys. Lett.*, 2009, **95**, 171905.
12 D. Sawaki, W. Kobayashi, Y. Moritomo and I. Terasaki, *Appl. Phys. Lett.*, 2011, **98**(8), 081915.
13 X. Zhang, P. Tong, J. Lin, K. Tao, X. Wang, L. Xie, W. Song and Y. Sun, *Phys. Rev. Appl.*, 2021, **16**, 014031.
14 R.-s Nakayama and T. Takeuchi, *J. Electron. Mater.*, 2015, **44**, 356–361.
15 A. Arora, T. Hori, T. Shiga and J. Shiomi, *Phys. Rev. B*, 2017, **96**, 165419.
16 H. Kang, F. Yang and J. J. Urban, *Phys. Rev. Appl.*, 2018, **10**, 024034.
17 K. Garcia-Garcia and J. Alvarez-Quintana, *Int. J. Therm. Sci.*, 2014, **81**, 76–83.
18 R. Shrestha, Y. Luan, X. Luo, S. Shin, T. Zhang, P. Smith, W. Gong, M. Bockstaller, T. Luo and R. Chen, *Nat. Commun.*, 2020, **11**, 4346.
19 T. Swoboda, K. Klinar, S. Abbasi, G. Brem, A. Kitanovski and M. M. Rojo, *iScience*, 2021, **24**(8), 102843.
20 K. Hirata, T. Matsunaga, S. Singh, M. Matsunami and T. Takeuchi, *J. Electron. Mater.*, 2020, **49**, 2895–2901.
21 Z. Meng, R. Gulfam, P. Zhang and F. Ma, *Int. J. Heat Mass Transfer*, 2020, **147**, 118915.
22 L. Zhang, J.-T. Lü, J.-S. Wang and B. Li, *J. Phys.: Condens. Matter*, 2013, **25**, 445801.
23 N. A. Roberts and D. Walker, *Int. J. Therm. Sci.*, 2011, **50**, 648–662.
24 X.-K. Chen, M. Pang, T. Chen, D. Du and K.-Q. Chen, *ACS Appl. Mater. Interfaces*, 2020, **12**, 15517–15526.
25 B. Li, L. Wang and G. Casati, *Phys. Rev. Lett.*, 2004, **93**, 184301.
26 A. Fiorino, D. Thompson, L. Zhu, R. Mittapally, S.-A. Biehs, O. Bezencenet, N. El-Bondry, S. Bansropun, P. Ben-Abdallah and E. Meyhofer, *ACS Nano*, 2018, **12**, 5774–5779.
27 H. Wang, S. Hu, K. Takahashi, X. Zhang, H. Takamatsu and J. Chen, *Nat. Commun.*, 2017, **8**, 15843.
28 X.-K. Chen, Z.-X. Xie, W.-X. Zhou, L.-M. Tang and K.-Q. Chen, *Carbon*, 2016, **100**, 492–500.
29 G. Wu and B. Li, *Phys. Rev. B: Condens. Matter Mater. Phys.*, 2007, **76**, 085424.
30 R. Powell, C. Ho and P. Liley, *Thermal Conductivity of Selected Materials*, US Government Printing Office, Washington, DC, 1966.
31 R. A. Matula, *J. Phys. Chem. Ref. Data*, 1979, **8**, 1147–1298.
32 M. Chowdhuri and Z. Xia, *Composites, Part B*, 2013, **44**, 253–259.
33 A. Lendlein and S. Kelch, *Angew. Chem., Int. Ed.*, 2002, **41**, 2034–2057.
34 T. Xie, *Nature*, 2010, **464**, 267–270.
35 C. Qian, Y. Dong, Y. Zhu and Y. Fu, *Smart Mater. Struct.*, 2016, **25**, 085023.
36 A. Lendlein, H. Jiang, O. Jünger and R. Langer, *Nature*, 2005, **434**, 879–882.
37 Y. Liu, H. Lv, X. Lan, J. Leng and S. Du, *Compos. Sci. Technol.*, 2009, **69**, 2064–2068.
38 Y. Ge, H. Wang, J. Xue, J. Jiang, Z. Liu, Z. Liu, G. Li and Y. Zhao, *ACS Appl. Mater. Interfaces*, 2021, **13**, 38773–38782.
39 S. Sun, C. Chen, J. Zhang and J. Hu, *RSC Adv.*, 2023, **13**, 3155–3163.
40 Y. Xia, Y. He, F. Zhang, Y. Liu and J. Leng, *Adv. Mater.*, 2021, **33**, 2000713.
41 F. Zhang, Y. Xia, Y. Liu and J. Leng, *Nanoscale Horiz.*, 2020, **5**, 1155–1173.
42 M. Uyan and M. S. Celiktas, *ACS Omega*, 2023, **8**, 15003–15016.
43 M. Wang, Q. Zhang, Y. Bo, C. Zhang, Y. Lv, X. Fu, W. He, X. Fan, J. Liang and Y. Huang, *Nano-Micro Lett.*, 2021, **13**, 124.
44 Q. Mu, C. K. Dunn, L. Wang, M. L. Dunn, H. J. Qi and T. Wang, *Smart Mater. Struct.*, 2017, **26**, 045008.
45 G. Fei, G. Li, L. Wu and H. Xia, *Soft Matter*, 2012, **8**, 5123–5126.
46 S. Choi, S. Jang, S. H. Yoo, G. W. Lee and D. Choi, *Polymers*, 2024, **16**, 2425.
47 L. Ma, J. Zhao, X. Wang, M. Chen, Y. Liang, Z. Wang, Z. Yu and R. C. Hedden, *Polymer*, 2015, **56**, 490–497.
48 S. Bistac, P. Kunemann and J. Schultz, *Polymer*, 1998, **39**, 4875–4881.
49 B. Tatár and L. Mészáros, *Polym. Bull.*, 2024, **81**, 6311–6323.
50 S. Bae and S. Baik, *Sens. Actuators, A*, 2024, **372**, 115343.
51 C. Granqvist and O. Hunderi, *Phys. Rev. B: Condens. Matter Mater. Phys.*, 1978, **18**, 1554.

52 K.-Y. Chun, Y. Oh, J. Rho, J.-H. Ahn, Y.-J. Kim, H. R. Choi and S. Baik, *Nat. Nanotechnol.*, 2010, **5**, 853–857.
53 S. A. Abdul Jaleel, T. Kim and S. Baik, *Adv. Mater.*, 2023, **35**, 2300956.
54 T. L. Bergman, *Fundamentals of heat and mass transfer*, John Wiley & Sons, 2011.
55 A. A. Jan, D. Suh, S. Bae and S. Baik, *Nanoscale*, 2018, **10**, 17799–17806.
56 D. Suh, C. M. Moon, D. Kim and S. Baik, *Adv. Mater.*, 2016, **28**, 7220–7227.
57 D. Suh, S. Lee, C. Xu, A. A. Jan and S. Baik, *Phys. Chem. Chem. Phys.*, 2019, **21**, 2453–2462.
58 H. Nobuoka, O. Urakawa and T. Inoue, *Polym. J.*, 2025, **57**, 995–1002.
59 Y. Xin, J. Zhou, R. Tao, X. Xu and G. Lubineau, *ACS Appl. Mater. Interfaces*, 2018, **10**, 33507–33515.
60 ASTM E1862, Standard Practice for Measuring and Compensating for Reflected Temperature Using Infrared Imaging Radiometers (American Society for Testing and Materials International, West Conshohocken, 2018).
61 ASTM E1933, Standard Practice for Measuring and Compensating for Emissivity Using Infrared Imaging Radiometers (American Society for Testing and Materials International, West Conshohocken, 2018).
62 Y. Guo, Y. Chen, Q. Yu, H. Liu, H. Li and Y. Yu, *Chem. Eng. J.*, 2023, **470**, 144212.
63 H. Kim, I. Cha, Y. Yoon, B. J. Cha, J. Yang, Y. D. Kim and C. Song, *ACS Sustainable Chem. Eng.*, 2021, **9**, 6952–6961.

